

Combination of rGO/S, N/TiO₂ for the Enhancement of Visible Light-Driven Toluene Photocatalytic Degradation

Birgitta Narindri Rara Winayu

National Cheng Kung University

Wan-Hua Mao

National Cheng Kung University

Hsin Chu (✉ chuhsin@mail.ncku.edu.tw)

National Cheng Kung University

Research

Keywords: Photocatalyst, Titanium oxide, toluene, non-metallic doping, graphite oxide

Posted Date: October 5th, 2021

DOI: <https://doi.org/10.21203/rs.3.rs-934278/v1>

License:  This work is licensed under a Creative Commons Attribution 4.0 International License. [Read Full License](#)

Abstract

Toluene is one type of common volatile organic compound (VOC) that is produced by daily products and is harmful to human health. Therefore, the degradation of toluene is critical to improving indoor air quality value. Photocatalytic degradation is considered an efficient and safe method to convert toluene into water and carbon dioxide without the formation of a secondary pollutant. Performance improvement of TiO_2 , a typically applied photocatalyst, has advantages in light absorption and electron transfer process. In this study, the TiO_2 improvement was carried out by the doping of sulfur and nitrogen (S, N) elements along with various reduced graphene oxide (rGO). The composition of $0.1\text{wt\%rGO/S}_{0.05}\text{N}_{0.1}\text{TiO}_2$ performed higher photocatalytic degradation of toluene due to the elevation of specific surface area, formation of oxygen-containing functional group, and chemical defect structure. However, a higher amount of rGO addition creates the shielding effect and inhibits the light penetration. Moreover, the relative humidity and applied temperature influence the photocatalytic activity through the competitive adsorption or increase the collisions frequency, respectively. During the photocatalytic degradation using $0.1\text{wt\%rGO/S}_{0.05}\text{N}_{0.1}\text{TiO}_2$, toluene will be converted into benzyl alcohol, benzaldehyde, benzoic acid, water, and carbon dioxide.

1. Introduction

The average 86–87 % of human activities were spent in the indoor environment, thus the quality of air environment is important [1]. Various types of volatile organic compounds (VOCs), including toluene have the potency to reduce the indoor air quality value. Toluene, an aromatic hydrocarbon, generally found in the various products such as catalytic reforming and steam cracking of petroleum fractions, direct coal liquefaction products, and coal aromatics [2]. Toluene is commonly used as the solvent, and has the clear, colorless, volatile, highly flammable liquid with a sweet sharp aromatic odor [3]. The removal of toluene is critical due to its damage as a carcinogenic agent, affecting nervous system, damaging liver, kidneys, and lungs with several symptoms such as fatigue, headache, vertigo, and ataxia [4].

Various strategies have been involved in the VOCs control technologies like thermal, biological, or catalytic oxidation, condensation, adsorption, and absorption. However, most of the strategies have the potency to create the secondary pollutant, require high cost and energy, or not effective for the low concentration pollutant [5–7]. Photocatalytic degradation is a potential strategy for the removal of indoor air pollution with low cost and energy consumption, efficient for the low pollutant concentration. TiO_2 is a typical photocatalyst nanoparticle that has been widely used for the organic compounds decomposition [8] or even in the water remediation, super capacitor, porous adsorbent supports, and sensor devices [9]. However, TiO_2 application has the limitation in visible light utilization, and recombination rate of photogenerated electron-hole pairs. TiO_2 utilizes UV illumination with the wavelength lower than 388 nm due to the wide bandgap (3.2 eV). Moreover, the rapid electron-hole pairs recombination will cause the low electron concentration in conduction band and reduce photocatalytic efficiency. Therefore, the modification of TiO_2 is needed to improve its photocatalytic reaction [10].

Doping metal elements on the TiO_2 surface increases the capability to absorb visible lights through the formation of traps for photo-induced electron or holes that leads the electron to a reduction state during the photocatalytic process [11]. On the other side, the non-metallic element doping inhibits the recombination of photogenerated electron-hole pairs of TiO_2 [12]. Sulfur can be doped as an anion and replace the lattice oxygen in TiO_2 . C-doping, for example, upon substitution of oxygen with carbon atoms presents new energy states in TiO_2 band gap, that are responsible for visible absorption [13]. Moreover, N-doping results in the formation of surface oxygen vacancies [14].

Recently, carbon-doped TiO_2 is a promising photocatalyst candidate because carbon is not only cheaper than the noble metal, but also shows good conductivity and strong absorption of light, which contributes to effective photo-degradation of pollutants [15]. In addition, the TiO_2 -graphene composites have greatly improved the photocatalytic activity due to extraordinary high electron mobility of graphene. Graphene in the composites becomes a sink of electrons from TiO_2 because of its lower Fermi level than the minimum conduction band of TiO_2 . Therefore, graphene facilitates the interface charge separation and hinders electron-hole recombination. Furthermore, in TiO_2 -graphene hybrid, the graphene plays an important role in extending the visible light absorbance and suppressing the charge carrier's recombination due to the transfer of electrons from TiO_2 surface to graphene [16].

Aim of this study is to observe the performance enhancement of TiO_2 doped with non-metallic elements (S, and N), and various concentration of reduced graphene oxide (rGO). Toluene was chosen as the targeted pollutant for the study of indoor air pollution control using photocatalytic degradation. Moreover, the study of influence from various environmental conditions were also carried out along with the kinetic study and proposed degradation mechanism.

2. Experimentals

2.1 Production of nanocomposite photocatalyst

Graphite oxide was prepared previously using the Hummer method [17] where 1 g graphite flakes, 0.5 g NaNO_3 and 23 mL H_2SO_4 were stirred together in an ice bath for 1 hour. KMnO_4 (3 g) then slowly added under the stirring and the temperature that kept at below 20 °C for 30 min before moved to the higher temperature water bath (35 °C) and continue the stirring process for 24 h. Subsequently, 46 mL of water was then added into the above mixture at 95 °C during a period of 1 h. Finally, the suspension was diluted by adding 130 mL water and 12 mL H_2O_2 (35 wt%) at room temperature and stirred for 30 minutes. The unexfoliated graphite oxide in mixture solution was removed by repeated centrifugation and rinsing (using 5–10 % HCl and water). And the final product was freeze-dried for the storage period.

Photocatalyst was prepared under the solvothermal method where TTIP as the Ti-precursor, thiourea ($\text{CH}_4\text{N}_2\text{S}$) as the sulfur-nitrogen-precursor (S, and N), and graphite oxide were used. S, and N elements was prepared with the amount of 5 mol% and 10 mol%, respectively for all various of observed graphite oxide concentration. 0.039 g graphite oxide was added into 20 mL ethanol and put under ultrasonic oscillation for 1 h to form the graphene oxide. Further, various

concentration of graphite oxide will be added in the ratio of weight% (wt%) in the range of 0.01–1 wt%. Separately, 15 mL TTIP and 0.186 g thiourea were added into 20 mL ethanol. Both graphene oxide and TTIP-thiourea solution will be further mixed and supplemented by 100 mL deionized water under continuous stirring for 30 min. Afterwards, adequate amount of nitric acid (65 wt %) was added to let the pH of the sol remain at 2 and be further stirred until the gel formed at 70°C for 30 min. Produced gel will be treated in a Teflon-lined stainless steel and autoclaved at 180 °C for 12 h before the drying process at 70 °C and storage period.

2.2 Characterization analyses of photocatalyst

Various analyses to observe physical and chemical properties of the synthesized photocatalyst were carried out. Phase transformation analysis of the photocatalyst was carried out using thermogravimetric/differential thermal analysis (TG/DTA) (Pyris Diamond TG/DTA, Perkin Elmer) with the temperature range of 50–850 °C and heating rate of 10 °C min⁻¹.

X-ray powder diffraction spectroscopy (XRD) (Rigaku X-ray Diffraction Model D/MAS IIIV) was implemented to determine the dominant crystallite phase. Detailed information of crystal structures was analyzed by MDI Jade 5.0. During the XRD analysis, Cu K α radiation in the range of 5–80 ° with a scan rate of 2 ° min⁻¹ was applied while the particle sizes and interplanar distance of the photocatalyst were estimated by the Scherrer equation and Bragg's law. Furthermore, to support the crystallite properties analysis, Raman spectroscopy (Tokyo Instruments, Nanofinder 30) was also applied for the determination of degree ordering and crystallinity.

Porous properties and specific surface area analysis were observed using Brunauer-Emmet-Teller (BET) analysis using nitrogen multilayer adsorption method. Surface properties of the photocatalyst were observed using scanning electron microscopy (SEM) (JEOL JSM-6700F). Moreover, transmission electron microscopy (TEM) (JEOL-2100F CS STEM) was used to analyze the Crystal structure through its diffraction pattern.

Molecular structure of the chemical functional groups of organic compounds in the photocatalyst was observed using Fourier transform infrared spectroscopy (FTIR) (Perkin Elmer Spectrum One B) equipped with a KBr beam splitter. Deeper observation on the photocatalyst band gap was carried out by the UV-visible spectrometry (Lamda 35, Perkin Elmer) equipped with and integrating sphere. The spectra were collected at room temperature and standard atmospheric air pressure within wavelengths of 250–700 nm. Furthermore, the binding energy analysis was carried out using X-ray photoelectron spectroscopy (XPS) (ULVAC-PHI 500 Versa Probe ESCA) with the Al K α -radiation (1,486 eV) as the source. The binding energies were calibrated with reference to C 1s at 285 eV.

2.3 Synthesized photocatalyst for the degradation of toluene

Photocatalytic degradation study was carried out in the plug flow reactor system (please refer to Figure S1) under the temperature of 25 °C, 60 % relative humidity value, 30 s resident time, and 2.0 ppm initial toluene concentration as the targeted pollutant. Toluene was supplied in a simulated gas system that consist of mixer, cylinders, and syringe pump with the air (O₂:N₂ = 21:79) for the purging process.

Synthesized photocatalyst (0.5 g) mixed with 10 mL anhydrous alcohol under continuous stirring for 24 h before coated on the inner surface of a pyrex glass reaction tube with the size of 15.5 cm length, 7.5 cm interior diameter, and 0.5 cm thickness. Oven-drying process will be applied to the pyrex tube with the temperature of 120 °C and installed in the plug flow reactor system. In order to create a steady still construction and prevent the leakage or interference from the other light source, the reactor was placed in a stainless steel structure. Vaporized toluene was supplied to be photocatalytic degraded by the synthesized photocatalyst using commercial fluorescent lamp (FL-10D, 10W, wavelength range of 360–700 nm with a peak λ = 436 nm and the light intensity was 2.5 mW cm⁻²) as the light source in the middle of pyrex tube. Light intensity was measured using luciferase spectrometer (Jasco FP-6200). Concentration of toluene was monitored online using gas chromatography-flame ionization detector (GC-FID) during the photo-degradation process.

Photocatalyst with the best toluene degradation performance will be further applied in the photocatalytic activity under various environmental conditions, including initial toluene concentration (1.0–4.0 ppm), temperature (25–45 °C), resident time (5–30 s), and relative humidity (5–80 %).

2.4 Kinetic study and byproducts analysis

Kinetic study of the relationship between reactants and operating parameters was carried out using Langmuir-Hinshelwood (L-H) modeling for the application of 0.1wt% rGO/S_{0.05}N_{0.1}TiO₂. An experimental design is performed using independent variables such as the temperature, humidity, residence time and toluene concentration. The data regression by the Langmuir-Hinshelwood kinetic model (please refer to Table 2) can provide the values of the kinetic constant, k, for a first order reaction and the adsorption constants, K_A and K_W. Moreover, FTIR and gas chromatography-mass spectrometry (GC-MS) instruments also applied to examine the generated byproducts and predict the photocatalytic degradation mechanism.

Table 2
Applied parameter comparison with other studies

Parameter	Best Value	Parameter range	Reference
Inlet concentration (ppm)	1	1–4	In this study
	2	2–10	(Tsai and et al., 2008)
Temperature (°C)	45	25–45	In this study
	35	15–35	(Tsai and et al., 2008)
Relative humidity (%)	0	0–80	In this study
	20	0–50	(Mamaghani et al., 2018)
Residence time (s)	30	5–30	In this study
	20	8.5–20	(Tsai and et al., 2008)

3. Results And Discussion

3.1 Photocatalyst Properties

Crystallite properties of synthesized photocatalyst was analyzed using XRD, and the results were shown in Fig. 1a, supported by Table 1. The presence of rGO can be noticed with a wide peak at around 25.5°. Moreover, the disappearance of the (0 0 2) plane of graphite oxide at 11.1° also indicates the reduction of graphite oxide to rGO by the solvothermal method [18]. The peaks located at 25.3 °, 36.9 °, 37.8 °, 48.0 °, 53.9 °, 55.1 °, 62.7 °, 68.8 °, 70.3 ° and 75.0 ° can be indexed to the (1 0 1), (1 0 3), (0 0 4), (2 0 0), (1 0 5), (2 1 1), (2 0 4), (1 1 6), (2 2 0) and (2 1 5) crystal planes, respectively, of the anatase TiO₂. However, the diffraction patterns of rGO/TiO₂ composites almost coincide with that of bare TiO₂. This is because of the overlap of characteristic peak (002 plane) of rGO at around 25 ° with 101 plane reflection of TiO₂ at around same 2θ value [19, 20]. Moreover, XRD pattern reveals no sulfur phase or S containing compounds in the S-doped samples owing to the low content of sulfur. The particle sizes of S, N, and graphene doped TiO₂ vary with various doping amounts. However, the lattice parameters *a* and *c* remain constant. It indicates that dopants in TiO₂ do not affect the photocatalytic properties of the nanoparticles and charge balance in the anatase lattice [21].

Table 1. XRD, raman, and BET analyses results for the characterization of crystal, band gap, and pores.

Sample	XRD						Raman				BET			
	crystal phase	Particle size	Crystallite size	Lattice parameter			Absorbance Spectra		Reflectance Spectra		Surface area	Pore volume	Pore size	
				Anatase (%)	D (nm)	d (nm)	<i>a</i> (Å)	<i>c</i> (Å)	c/a	Band gap (eV)	Band edge wavelength (nm)	Band gap (eV)	Band edge wavelength (nm)	
TiO ₂		100	10.45	0.3494	3.771	9.373	2.486	3.19	389	2.55	486	155.1	0.297	7.64
S _{0.05} N _{0.1} TiO ₂		100	10.47	0.3498	3.776	9.374	2.483	3.06	405	2.54	488	169.2	0.283	6.68
0.01wt%rGO/S _{0.05} N _{0.1} TiO ₂		100	10.60	0.3498	3.778	9.437	2.498	3.03	410	2.53	490	149.0	0.288	7.73
0.1wt%rGO/S _{0.05} N _{0.1} TiO ₂		100	10.55	0.3494	3.779	9.431	2.495	2.95	420	2.52	492	161.7	0.297	7.35
0.5wt%rGO/S _{0.05} N _{0.1} TiO ₂		100	10.11	0.3502	3.780	9.410	2.489	2.76	450	2.51	494	160.7	0.289	7.19
1wt%rGO/S _{0.05} N _{0.1} TiO ₂		100	11.11	0.3490	3.773	9.388	2.488	2.73	455	2.50	496	143.4	0.276	7.70

^a Total pore volume of pores at P/P₀ = 0.99 for single point adsorption

^b Average pore width (4V/A by BET)

According to the FTIR spectra results in Fig.1b, the peak at 1,650 cm⁻¹ arises from the C=C stretch of alkenes. In the case of photocatalysts containing TiO₂ nanocomposites, a Ti-O-Ti vibration correlated to the slope between 500 and 1,000 cm⁻¹ can be recognized, which is attributed to the TiO₂ nanoparticles. A peak around 793 cm⁻¹ should be likely owing to the vibration of Ti-O-C bond which confirms the formation of chemical bond between the rGO and TiO₂ nanoparticles. Therefore, the large range of Ti-O-Ti vibration and the vibration of Ti-O-C are hard to distinguish [19, 22]. The FTIR peaks observed at 1,257 cm⁻¹

and 1,049 cm⁻¹ are assigned to the SO stretching mode and S–O stretching vibration, respectively [23]. However, after solvothermal process the bands related to oxygen-functional groups of graphene oxide are still present in the photocatalysts spectra suggesting that reduction of graphite oxide is not complete [24, 25].

Figure 1 also displays the raman spectra of the synthesized photocatalyst. Raman spectra exhibits two characteristic Raman bands, D band at 1,350 cm⁻¹ and G band at 1,600 cm⁻¹. The D band is assigned to edge or in-plane sp³ defects and disordered carbon, whereas the G band arises from the in-plane vibration of ordered sp²-bonded carbon atoms [26]. The I_D/I_G intensity ratio of reduced graphene oxide increases compared with that of graphite oxide, which suggests the structural change due to the removing of functional groups [27]. Furthermore, all photocatalysts exhibiting a Raman peak pattern similar to the characteristic feature of anatase structured TiO₂. The peaks at 144, 398, 515, and 633 cm⁻¹ can be assigned as the E_{g1}, B_{1g}, A_{1g}, and E_{g2}, respectively. These are arising from the external vibration of the anatase structure, which indicates that an anatase phase was formed in the photocatalysts [26]. Moreover, according to the supportive raman result in Table 1, the value of I_D/I_G increases when rGO content increases.

Table 1 also presented the porous structure of synthesized photocatalyst using BET analysis. The pore sizes of all photocatalysts are in the range of 6–7 nm, within the range of the mesoporous (2–50 nm). In addition, all photocatalysts can be attributed to the type IV curve and are tended to hysteresis loops [20]. The BET surface area of the different weight percent of rGO/S_{0.05}N_{0.1}TiO₂ samples significantly decreases from 161.7 to 143.4 m² g⁻¹ with increasing rGO content. However, the BET surface area of the 0.01wt% rGO/S_{0.05}N_{0.1}TiO₂ is relatively low compared to that of bare TiO₂ (155.1 m² g⁻¹). Thus, surface area and porosity are mainly dominated by the TiO₂ component [28].

The surface properties of synthesized photocatalyst were analyzed using SEM and TEM as displayed in Fig. 2. TiO₂ composites are dispersed on the surface of rGO and some TiO₂ composites enter into the interlayers of rGO [29], this structure support the efficient electron collection through rGO sheets during the process [30]. TiO₂ and S doped TiO₂ nanoparticles have a quasi-spherical shape like morphology with an average size of 10–15 nm, which is in agreement with the calculated results from the Scherrer's equation [31]. Increasing rGO content in the photocatalyst form bigger aggregate.

XPS instrument was applied to observe the chemical and electronic states of the elements and chemical bonding on the surface of photocatalysts as shown in Fig. 3. Ti 2p XPS spectra for TiO₂ indicate the peaks centered at 458.4 and 464.0 eV corresponding to Ti 2p_{3/2} and Ti 2p_{1/2}, respectively. These peaks are occurred due to spin-orbital splitting photoelectrons in the Ti⁴⁺ valence state suggesting a normal state of Ti⁴⁺. In addition, Ti-C bond can be attributed to the formation of a bond between Ti and C atoms on the TiO₂ composites as confirmed by analysis of the XPS core level of C 1s [32]. Under the C 1s spectra identified signals at 284.5, 285.1, 286 and 288.6 eV were related to C = C, C-C, C-O and -COOH bonds, respectively [33]. The O 1s core level peaks can be observed at 529.7 eV (Ti-O-Ti/ Ti-O-C), 530.2 eV (C = O), 531.5 eV (C-O) and 532.7 eV (O-H) [34], while the carbon materials has oxygen-containing species at 531.6 eV (-C=O-). The S 2p peaks at 168.3 and 169.3 eV are due to Ti-S and C-S bonds, respectively. The N 1s peak at 400.2 eV is associated with Ti-N bonding, which clearly demonstrates that nitrogen atoms were doped into the anatase lattice and replaced a small portion of oxygen atoms during the solvothermal process. Hence, the XPS results clearly confirm the presence of co-doped N and S on the lattices of rGO/TiO₂ photocatalysts [34].

The TG/DTA curves for the synthesized photocatalysts was presented in Fig. 4. In the range of 180 to 380°C, about 9.0 % weight is lost from TiO₂ which is attributed to the decomposition of organic compounds. The amorphous precursor is converted to the anatase phase as the temperature increases from 425 to 500 °C. It is observed that there is no weight loss above 500°C, indicating the onset of oxide formation and expected changes in the crystal. Above this temperature the TGA and DTA curves no longer exhibit any peak. Moreover, S_{0.05}N_{0.1}TiO₂, primary weight loss occurs at temperature range of 50°C to 140°C, which can be associated with the vaporization of adsorbed/absorbed H₂O and organics. The second region is in the range of 150–450°C, where the weight loss is about 10 % due to the removal of strongly bound water or surface hydroxyl groups. The third stage is from 450°C to 800°C, where the mass loss is due to oxidation of S and then mass the weight remains constant [35]. However, the photocatalyst with rGO has a higher weight loss than that without rGO in temperature ranges of 150–250 °C and 600–730 °C. The weight loss, between 200°C and 450°C, can be attributed to the decomposition of the remaining organic compounds formed during the synthesis and partial oxygen-containing functional groups in the reduced graphene oxide. The weight loss in the range of 450–650°C depicts the oxidation of carbon scaffold of the rGO [36].

Figure 5 displays the optical properties of photocatalyst as the result from UV-visible spectrometry analysis. The results show a noticeable shift of absorption edge which are demonstrated in S, N-doped TiO₂ samples compared with bare TiO₂ [19]. For incident wavelengths in the range 200–800 nm, rGO/S_{0.05}N_{0.1}TiO₂ composites might be photocatalytically active under visible irradiation [37]. The band gap energies of the samples, estimated by converting the reflectance spectra to absorption Kubelka-Munk units. The result of bandgap calculation was shown in Fig. 5b and reveal that the energy gap decreases with increasing wt% of rGO in the composites. This phenomenon occurred due to the Ti-O-C bonds of rGO/TiO₂ nanocomposites between TiO₂ nanoparticles and rGO nanosheets are able to cause an intimate interaction and decrease the band gap [19].

3.2 Visible light-driven photocatalytic degradation of toluene

Toluene in the initial concentration of 2 ppm was supplied as the pollutant to be degraded by various synthesized photocatalyst under the relative humidity value of 60 % at the temperature of 25 °C. Figure 6 displays the toluene conversion and reaction rate during the photocatalytic degradation. The results indicate that 0.1wt%rGO/S_{0.05}N_{0.1}TiO₂ has the best photocatalytic activity among all rGO doping ratios. It is found that co-doped nitrogen and sulfur (N, S) would increase the conversion rate due to an increase in the absorption of visible light [38]. Additional rGO content in the photocatalyst enhance the photocatalytic activity due to the promotion of surface •OH radicals and the interference in •O₂⁻ radicals' generation [38]. However, adding excessive or less rGO may increase collision opportunities between electrons and holes which causes faster electron-hole pairs recombination [39]. According to the results, 0.1wt%rGO/S_{0.05}N_{0.1}TiO₂ will be further implemented for the study of parameters influence, and kinetic analysis.

3.3 Photocatalytic activity under various applied environmental conditions

Photocatalyst with the composition of $0.1\text{wt\%rGO/S}_{0.05}\text{N}_{0.1}\text{TiO}_2$ was chosen for the parameters test under various initial toluene concentration (1–4 ppm), temperature (25–45 °C), relative humidity (0–80 %), and retention time (5–30 s). The results of toluene conversion under various parameters were displayed in Fig. 7. The toluene degradation efficiency was reduced under the supply of higher initial pollutant concentration as seen in Fig. 7a and 7b. The relationship between pollutant concentration and reaction rate may follow the Langmuir-Hinshelwood (L–H) model [40], and considering principles of catalytic reactions, at low pollutant concentration, the reaction rate increases with pollutant concentration until it reaches a region where the reaction rate becomes independent of concentration. However, at higher concentration due to the deposition of refractory reaction intermediates on photocatalyst surface and loss of active sites the reaction rate dramatically drops [41]. Numerous studies observed the photocatalytic performance at low pollutant concentration and presented the improvement of reaction rate at higher VOC concentration, but reduction of removal efficiency and mineralization [41].

Moreover, higher relative humidity (RH) value reduced the photocatalytic activity for toluene degradation. The water vapor content in the gaseous effluent created competitive adsorption with toluene molecule on the photocatalyst active sites [42]. However, the presence of 1 % RH displayed higher conversion compared to the 0 % and indicated that the water vapor also induces the photocatalytic activity due to the formation of hydroxyl radicals [41].

Under the higher applied temperature, toluene photocatalytic degradation was also increased due to the exothermic and equilibrium reaction in elementary steps and influenced the overall reaction rate [43]. Temperature not only affects the reaction kinetics but also the adsorption of the gas-phase compounds on the photocatalyst and influenced the amount of adsorbed pollutants on the reaction surface thus it may lower the reaction rate under the mass transfer limit process [40]. According to previous study, the optimum temperature was found in the range of 40–50 °C. Under low temperature, products desorption will be occurred due to the slower reaction than the degradation on the surface or the reactants adsorption. Nevertheless, higher temperature, adsorption of toluene on the photocatalyst surface also become a limitation [44].

The direct effects that flow rates had on retention time indicate that mass transfer plays an important role and limits the rate of oxidation as seen on Fig. 7g and 7h. Higher flow rates in the reactor and the decreased retention time results in a decreased amount of photocatalytically decomposed pollutants [45]. The results show that the conversion of toluene increases with an increase of retention time. As the airflow rate increases, the residence time of VOC molecules inside the reactor decreases which leads to a reduction in the adsorption of the pollutant and lower conversion [41]. However, the reaction rate decreases with an increase of retention time. The importance of adsorption capacity increases as the residence time decreases, and adsorption may be more important than photocatalytic activity at a short residence time [46].

Table 2 displays the comparison of possible applied parameters using the synthesized photocatalyst in this study and other study. The combination of $0.1\text{wt\%rGO/S}_{0.05}\text{N}_{0.1}\text{TiO}_2$ in this study is applicable for the degradation of toluene even in low concentration. The wide range of RH value during the photocatalytic activity also become another advantage compared to the other study.

3.4 Photocatalytic kinetic analysis

In this study, Langmuir-Hinshelwood models 1–7 were used to simulate data generated from the kinetic experimental set as shown in Table 3 along with the simulation results after the fitting process with polymath software. The simulation results of model 4 are best suited to this study. Rate constant k of model 4 increases when the reaction temperature increases. However, adsorption constant K_w shows the opposite trend since a higher temperature would induce more species desorption from the photocatalyst surface. It is worth noting that the photocatalytic degradation rate relates to both reaction and adsorption constants, which have an impact on the final apparent reaction rate [47]. Therefore, the value of K_w is higher, the pollutant of toluene is more competitive with water.

Table 3

The results of reaction rate constants (k), formaldehyde adsorption equilibrium constants (K_A) and water vapor adsorption equilibrium constants (K_W) for Langmuir-Hinshelwood models 1–7.

Model	Reaction Rate Expression	Tem.	k	K_A	K_W	RSS	R^2
			(K)	(mol cm ⁻³ s ⁻¹)	(cm ³ mol ⁻¹)		
1		298	2.75E-10	1.02E+08	-	3.62E-20	0.92
		308	3.23E-10	9.89E+07	-	3.37E-20	0.93
		318	4.72E-10	8.30E+07	-	3.12E-20	0.93
2		298	9.41E-02	1.59E+00	1.36E+03	2.87E-23	0.00
		308	4.26E-01	7.18E+00	6.16E+03	9.26E-24	0.35
		318	4.19E-01	7.06E+00	6.05E+03	4.70E-24	0.77
3		298	9.97E-06	2.34E+03	1.87E+05	1.37E-24	0.89
		308	1.11E-05	2.58E+03	5.99E+04	9.90E-25	0.93
		318	1.29E-05	3.01E+03	7.24E+03	1.34E-24	0.93
4		298	4.27E-09	3.60E+07	1.25E+06	1.36E-24	0.96
		308	4.81E-09	3.30E+07	1.15E+06	1.68E-24	0.96
		318	5.55E-09	3.05E+07	1.08E+06	1.12E-24	0.95
5		298	2.89E-09	1.00E+07	1.06E+07	9.13E-25	0.93
		308	3.11E-09	1.05E+07	3.06E+07	8.93E-25	0.94
		318	3.49E-09	1.16E+07	1.66E+07	1.27E-24	0.94
6		298	9.57E-10	1.08E+07	3.02E+07	9.05E-25	0.93
		308	1.02E-09	3.07E+07	3.22E+07	8.93E-25	0.94
		318	1.13E-09	1.67E+07	3.58E+07	1.27E-24	0.94
7		298	8.16E-09	1.84E+04	6.19E+05	3.76E-24	0.70
		308	9.28E-09	1.89E+04	6.36E+05	4.76E-24	0.67
		318	1.26E-08	1.53E+04	6.35E+05	6.98E-24	0.66

Furthermore, the calculation using model 4 are shown in Table 4 where The activation energy of this photocatalytic reaction is 10.3 kJ mol⁻¹, the enthalpy of physisorbed toluene and water are - 5.3 and - 4.5 kJ mol⁻¹, respectively. The activation energy represents the dependence of the photocatalytic degradation rate on the temperature, and it takes into account only surface adsorption – desorption phenomena [48]. These results were supported by the 3D surface mesh diagram as shown in Fig. 8. According to Fig. 8, the model 4 can illustrate the experimental data well.

Table 4
Model 4 reaction rate constant and adsorption equilibrium constants from the suitable kinetic model.

Parameters	Units	Model 4
k'	mol cm ⁻³ s ⁻¹	3.15E-07
K'_A	$K^{0.5}$ cm ³ mol ⁻¹	7.46E+07
K'_W	$K^{0.5}$ cm ³ mol ⁻¹	3.52E+06
E_a	kJ mol ⁻¹	10.3
ΔH_A	kJ mol ⁻¹	-5.3
ΔH_W	kJ mol ⁻¹	-4.5

3.5 Mechanism of toluene photodegradation

Generated byproducts analysis during the photocatalytic degradation of toluene under 0 and 60 % RH using 0.1wt%rGO/S_{0.05}N_{0.1}TiO₂ for 8 h was shown in Fig. 9 along with the mineralization efficiency. As shown in Fig. 9, The peaks of 3,076 and 3,037 cm⁻¹ can be attributed to the C–H stretching vibration of aromatic ring, while 2,937 and 2,881 cm⁻¹ could be ascribed to the symmetric and asymmetric C–H stretching vibrations of methyl groups, respectively. The bands at the range of 1,000–1,260 cm⁻¹ are corresponding to C–O stretching vibration. In addition, the vibration of aromatic ring is associated with bands at

1,609 and 1,496 cm⁻¹. Upon irradiation, the two bands at 2,360 and 2,338 cm⁻¹ corresponding to CO₂ increase obviously. However, some intermediate products also form in the progress of photocatalytic reaction under visible-light irradiation. The bands at around 1,685 and 1,671 cm⁻¹, referred to the stretching vibration of the aldehydes, demonstrate the formation of benzaldehyde. Furthermore, the stretching vibrational (C = O) of carbonyl compounds in benzaldehyde are discovered in the bands which located at 1,541 and 1,508 cm⁻¹. The peaks centered at 1,653 and 1,636 cm⁻¹ are related to the C = C stretching vibrations for benzoic acid. And the asymmetric stretching vibration modes of the carboxylate group COO⁻ from benzoic acid are observed at 1,558 and 1,521 cm⁻¹. Moreover, the bands appeared at 1,473 and 1,457 cm⁻¹ are belong to the characteristic peaks of benzyl alcohol [38, 49, 50].

At 0% RH, C-H group, CO₂ and C-O binding can be found. However, these peaks cannot be found obviously. It's suggested that toluene may not be converted completely to CO₂ at high relative humidity, and the toluene conversion decreases with an increase of relative humidity. A higher humidity results in a lower toluene conversion due to the competitive adsorption of water with toluene. However, a dry condition can early convert toluene to CO₂, preventing the deactivation of photocatalysts, which is widely observed under higher humidity due to the partially oxidized species of toluene (such as benzaldehyde and benzoic acid) remaining on the catalyst surfaces.

For the analysis of mineralization ratio, the experiments were carried out at the retention time of 30 s, the inlet concentration of toluene 1 ppm, relative humidity 60 %, and ambient temperature 25 °C. It can be found that the conversion and mineralization efficiency gradually increase with decomposition time until a steady state occurs, which indicates that toluene is oxidized into CO₂ and H₂O. However, the conversion of toluene to CO₂ and H₂O is not 100 %, some intermediate products also form in the progress of photocatalytic reaction [51]. Nevertheless, the FTIR instrument could not detect the low concentration of CO₂ functional groups due to the incomplete conversion.

According to the result of FTIR and mineralization ratio analyses along with the previous study of Sleiman, Conchon [52], therefore the predicted photodegradation mechanism was illustrated in Fig. 10. The electrons and holes would react with O₂ and H₂O to generate a series of reactive oxygen species ($\cdot\text{OH}$, $\cdot\text{O}_2^-$) to partake photocatalytic reaction. Therefore, with the existence of $\cdot\text{OH}$ and $\cdot\text{O}_2^-$, it is speculated that gaseous toluene could be photo-oxidized to benzaldehyde initially, which proved in the FTIR results stretching vibrational (C = O) of carbonyl compounds in benzaldehyde. With the irradiation time increases, the benzaldehyde could be further photo-oxidized into benzoic acid, which proved in the FTIR results the asymmetric stretching vibration modes of the carboxylate group COO⁻ from benzoic acid. Finally, they will be degraded into CO₂ and H₂O to decrease the toxicity of toluene [53].

Based on the FTIR analysis of generated byproducts (please refer to Fig. 9), two competitive reaction pathways appear to occur depending on the RH level. The occurrence of two different pathways might be related to the competition of different active species and the adsorption modes of toluene on the TiO₂ surface. Under the absence of water vapor, the reaction is mainly initiated via an electron transfer from toluene to TiO₂ with the formation of an aromatic radical cation and a benzyl radical. Benzyl radical can then react with O₂ to form a benzylperoxy radical which decomposes thermally on the surface to give benzaldehyde and hydroxyl radical ($\cdot\text{OH}$). Meanwhile, the aromatic radical cation can also react with oxygen and form an aromatic bridged peroxy intermediate. Benzaldehyde can be further oxidized to benzoic acid which in turn decomposes on the TiO₂ surface giving rise to benzene and CO₂. The reaction proceeds by a series of oxidation steps by holes (h⁺), oxygen and $\cdot\text{OH}$ radicals at lesser extent, leading finally to the formation of CO₂.

4. Conclusion

The modification on TiO₂ photocatalyst was carried out by the addition of rGO and non-metal elements (S, and N). The particle TiO₂ attached to the rGO surface and interposed between the layers which promoted the elevation of specific surface area. Improvement of photocatalytic activity from the synthesized photocatalyst was achieved by the formation of chemical defects and bonding which introduce the oxygen-containing functional groups during the process. Moreover, the absorption spectra result of UV-visible analysis performed the improvement of visible light absorption intensity and reduction of bandgap from the addition of S and N elements. The rGO content itself also plays important role in the electron transport process with great capacity. However, excess rGO content will inhibit the light absorption, and in this study, 0.1 wt% of rGO is considered as the optimum composition for the addition in the photocatalyst material. The photocatalytic degradation of toluene is highly dependent on the RH value. A higher RH value will reduce photocatalytic degradation due to the competitive adsorption between water and toluene molecules on the photocatalyst surface. Higher collision frequency in the operation using higher temperature also enhanced the photocatalytic activity. The suitable kinetic modeling was achieved by the L-H model 4. During the photocatalytic degradation of toluene, the molecules will be converted into benzyl alcohol, benzaldehyde, benzoic acid, and carbon dioxide.

Declarations

Acknowledgements

The authors acknowledge appreciatively to the Ministry of Science and Technology, Taiwan, for the financial support on the research with project number of MOST (106-2221-E-006-017-MY3).

Author's Contribution

Birgitta Narindri Rara Winayu investigated the resources, provided data visualization and original draft writing, review & editing. Wan-Hua Mao provided methodology, resources investigation, data analysis and validation. Hsin Chu supported the conceptualization, methodology, supervision, project administration, funding acquisition, manuscript writing-review and editing.

Availability of Data and Material

All data in this study are generated and analyzed by our group during the examination and verification process.

Funding

Taiwan Ministry of Science and Technology (MOST 106-2221-E-006-017-MY3).

Competing Interest

The authors declare that they have no known competing financial interests or personal relationships that could have appeared to influence the work reported in this paper.

References

1. McNamara, M.L., et al., Reducing indoor air pollutants with air filtration units in wood stove homes. *Science of The Total Environment*, 2017. 592: p. 488-494.
2. Liu, J.-M., et al., Hydrodynamic cavitation for the enhancement of toluene disproportionation; study of the products distribution. *Chemical Engineering and Processing - Process Intensification*, 2018. 125: p. 34-43.
3. Luttrell, W.E. and T. Ngendahimana, Toxic tips: Toluene. *Journal of Chemical Health & Safety*, 2012. 19(3): p. 34-35.
4. Wu, H., et al., Performance and bacterial diversity of biotrickling filters filled with conductive packing material for the treatment of toluene. *Bioresource Technology*, 2018. 257: p. 201-209.
5. Fang, W., M. Xing, and J. Zhang, Modifications on reduced titanium dioxide photocatalysts: A review. *Journal of Photochemistry and Photobiology C: Photochemistry Reviews*, 2017. 32: p. 21-39.
6. Kamal, M.S., S.A. Razzak, and M.M. Hossain, Catalytic oxidation of volatile organic compounds (VOCs) – A review. *Atmospheric Environment*, 2016. 140: p. 117-134.
7. MiarAlipour, S., et al., TiO₂/porous adsorbents: Recent advances and novel applications. *Journal of Hazardous Materials*, 2018. 341: p. 404-423.
8. Gupta, S. and M. Tripathi, A review of TiO₂ nanoparticles. *Chinese Science Bulletin*, 2011. 56: p. 1639-1657.
9. Rahimi, N., R.A. Pax, and E.M. Gray, Review of functional titanium oxides. I: TiO₂ and its modifications. *Progress in Solid State Chemistry*, 2016. 44(3): p. 86-105.
10. Dolat, D., et al., Nitrogen-doped, metal-modified rutile titanium dioxide as photocatalysts for water remediation. *Applied Catalysis B: Environmental*, 2015. 162: p. 310-318.
11. Park, J.-Y., et al., Fabrication and characterization of metal-doped TiO₂ nanofibers for photocatalytic reactions. *Materials Letters*, 2013. 97: p. 64-66.
12. Khaki, M.R.D., et al., Application of doped photocatalysts for organic pollutant degradation - A review. *Journal of Environmental Management*, 2017. 198: p. 78-94.
13. Fotiou, T., et al., Assessment of the roles of reactive oxygen species in the UV and visible light photocatalytic degradation of cyanotoxins and water taste and odor compounds using C-TiO₂. *Water Research*, 2016. 90: p. 52-61.
14. Zhou, W., et al., Ultrasonic fabrication of N-doped TiO₂ nanocrystals with mesoporous structure and enhanced visible light photocatalytic activity. *Chinese Journal of Catalysis*, 2013. 34(6): p. 1250-1255.
15. Yu, C., et al., Sol-gel derived S,I-codoped mesoporous TiO₂ photocatalyst with high visible-light photocatalytic activity. *Journal of Physics and Chemistry of Solids*, 2010. 71(9): p. 1337-1343.
16. Khalid, N.R., et al., Carbonaceous-TiO₂ nanomaterials for photocatalytic degradation of pollutants: A review. *Ceramics International*, 2017. 43(17): p. 14552-14571.
17. Hummers, W.S. and R.E. Offeman, Preparation of Graphitic Oxide. *Journal of the American Chemical Society*, 1958. 80(6): p. 1339-1339.
18. Kumar, K.D., G.P. Kumar, and K.S. Reddy, Rapid Microwave Synthesis of Reduced Graphene Oxide-supported TiO₂ Nanostructures as High Performance Photocatalyst. *Materials Today: Proceedings*, 2015. 2(4): p. 3736-3742.
19. Chen, Y., et al., Facile fabrication of three-dimensional interconnected nanoporous N-TiO₂ for efficient photoelectrochemical water splitting. *Journal of Materials Science & Technology*, 2018. 34(6): p. 955-960.
20. Hao, N., et al., Multiple signal-amplification via Ag and TiO₂ decorated 3D nitrogen doped graphene hydrogel for fabricating sensitive label-free photoelectrochemical thrombin aptasensor. *Biosensors and Bioelectronics*, 2018. 101: p. 14-20.
21. Burns, A., et al., Neodymium ion dopant effects on the phase transformation in sol-gel derived titania nanostructures. *Materials Science and Engineering: B*, 2004. 111(2): p. 150-155.
22. Liu, C., et al., Hydrothermal synthesis of N-doped TiO₂ nanowires and N-doped graphene heterostructures with enhanced photocatalytic properties. *Journal of Alloys and Compounds*, 2016. 656: p. 24-32.
23. Sharotri, N. and D. Sud, A greener approach to synthesize visible light responsive nanoporous S-doped TiO₂ with enhanced photocatalytic activity. *New Journal of Chemistry*, 2015. 39(3): p. 2217-2223.
24. Aleksandrzak, M., et al., Effect of graphene thickness on photocatalytic activity of TiO₂-graphene nanocomposites. *Applied Surface Science*, 2015. 331: p. 193-199.

25. Yu, Z., et al., Preparation of graphene oxide modified by titanium dioxide to enhance the anti-corrosion performance of epoxy coatings. *Surface and Coatings Technology*, 2015. 276: p. 471-478.
26. Yadav, H.M. and J.-S. Kim, Solvothermal synthesis of anatase TiO₂-graphene oxide nanocomposites and their photocatalytic performance. *Journal of Alloys and Compounds*, 2016. 688: p. 123-129.
27. Zhang, L., et al., Aluminum/graphene composites with enhanced heat-dissipation properties by in-situ reduction of graphene oxide on aluminum particles. *Journal of Alloys and Compounds*, 2018. 748: p. 854-860.
28. Zhang, Y., et al., Graphene TiO₂ nanocomposites with high photocatalytic activity for the degradation of sodium pentachlorophenol. *Journal of Environmental Sciences*, 2014. 26(10): p. 2114-2122.
29. Jiang, T., et al., Preparation and photocatalytic property of TiO₂-graphite oxide intercalated composite. *Catalysis Communications*, 2012. 28: p. 47-51.
30. Dong, L., et al., Hydrothermal synthesis of mixed crystal phases TiO₂-reduced graphene oxide nanocomposites with small particle size for lithium ion batteries. *International Journal of Hydrogen Energy*, 2014. 39(28): p. 16116-16122.
31. Singaram, B., et al., Preparation of cerium and sulfur codoped TiO₂ nanoparticles based photocatalytic activity with enhanced visible light. *Journal of Photochemistry and Photobiology A: Chemistry*, 2017. 349: p. 91-99.
32. Ghasemi, S., et al., Plasmon enhanced photocatalytic activity of Au@TiO₂-graphene nanocomposite under visible light for degradation of pollutants. *Materials Research Bulletin*, 2017. 87: p. 40-47.
33. Cong, Y., et al., Carbon-doped TiO₂ coating on multiwalled carbon nanotubes with higher visible light photocatalytic activity. *Applied Catalysis B: Environmental*, 2011. 107(1): p. 128-134.
34. Brindha, A. and T. Sivakumar, Visible active N, S co-doped TiO₂/graphene photocatalysts for the degradation of hazardous dyes. *Journal of Photochemistry and Photobiology A: Chemistry*, 2017. 340: p. 146-156.
35. Boningari, T., et al., Novel one-step synthesis of sulfur doped-TiO₂ by flame spray pyrolysis for visible light photocatalytic degradation of acetaldehyde. *Chemical Engineering Journal*, 2018. 339: p. 249-258.
36. Suave, J., et al., TiO₂/reduced graphene oxide composites for photocatalytic degradation in aqueous and gaseous medium. *Journal of Photochemistry and Photobiology A: Chemistry*, 2017. 348: p. 326-336.
37. Martins, P.M., et al., TiO₂/graphene and TiO₂/graphene oxide nanocomposites for photocatalytic applications: A computer modeling and experimental study. *Composites Part B: Engineering*, 2018. 145: p. 39-46.
38. Li, X., et al., Graphene-based heterojunction photocatalysts. *Applied Surface Science*, 2018. 430: p. 53-107.
39. Xu, D., et al., Noble metal-free RGO/TiO₂ composite nanofiber with enhanced photocatalytic H₂-production performance. *Applied Surface Science*, 2018. 434: p. 620-625.
40. Mo, J., et al., Photocatalytic purification of volatile organic compounds in indoor air: A literature review. *Atmospheric Environment*, 2009. 43(14): p. 2229-2246.
41. Mamaghani, A.H., F. Haghigat, and C.-S. Lee, Photocatalytic degradation of VOCs on various commercial titanium dioxides: Impact of operating parameters on removal efficiency and by-products generation. *Building and Environment*, 2018. 138: p. 275-282.
42. Zadi, T., et al., Treatment of hospital indoor air by a hybrid system of combined plasma with photocatalysis: Case of trichloromethane. *Chemical Engineering Journal*, 2018. 349: p. 276-286.
43. Yamamoto, A., et al., Effects of reaction temperature on the photocatalytic activity of photo-SCR of NO with NH₃ over a TiO₂ photocatalyst. *Catalysis Science & Technology*, 2013. 3(7): p. 1771-1775.
44. Reza, K.M., A.S.W. Kurny, and F. Gulshan, Parameters affecting the photocatalytic degradation of dyes using TiO₂: a review. *Applied Water Science*, 2017. 7(4): p. 1569-1578.
45. Tsai, C.W., et al., Study on the indoor volatile organic compound treatment and performance assessment with TiO₂/MCM-41 and TiO₂/quartz photoreactor under ultraviolet irradiation. *J Air Waste Manag Assoc.*, 2008. 2008 Oct;58(10):1266-73. (1096-2247 (Print)).
46. Lv, K., et al., Fabrication of TiO₂ nanorod assembly grafted rGO (rGO@TiO₂-NR) hybridized flake-like photocatalyst. *Applied Surface Science*, 2017. 391(PartB): p. 218-227.
47. Hu, M., et al., Enhancement mechanism of hydroxyapatite for photocatalytic degradation of gaseous formaldehyde over TiO₂/hydroxyapatite. *Journal of the Taiwan Institute of Chemical Engineers*, 2018. 85: p. 91-97.
48. Parrino, F., et al., Influence of Adsorbed Water on the Activation Energy of Model Photocatalytic Reactions. *The Journal of Physical Chemistry C*, 2017. 121(4): p. 2258-2267.
49. Zhu, Z., F. Liu, and W. Zhang, Fabricate and characterization of Ag/BaAl₂O₄ and its photocatalytic performance towards oxidation of gaseous toluene studied by FTIR spectroscopy. *Materials Research Bulletin*, 2015. 64: p. 68-75.
50. Zhang, Z., et al., Hexagonal microspindle of NH₂-MIL-101(Fe) metal-organic frameworks with visible-light-induced photocatalytic activity for the degradation of toluene. *RSC Advances*, 2016. 6(6): p. 4289-4295.
51. Zou, T., et al., Full mineralization of toluene by photocatalytic degradation with porous TiO₂/SiC nanocomposite film. *Journal of Alloys and Compounds*, 2013. 552: p. 504-510.
52. Sleiman, M., et al., Photocatalytic oxidation of toluene at indoor air levels (ppbv): Towards a better assessment of conversion, reaction intermediates and mineralization. *Applied Catalysis B: Environmental*, 2009. 86(3): p. 159-165.

Figures

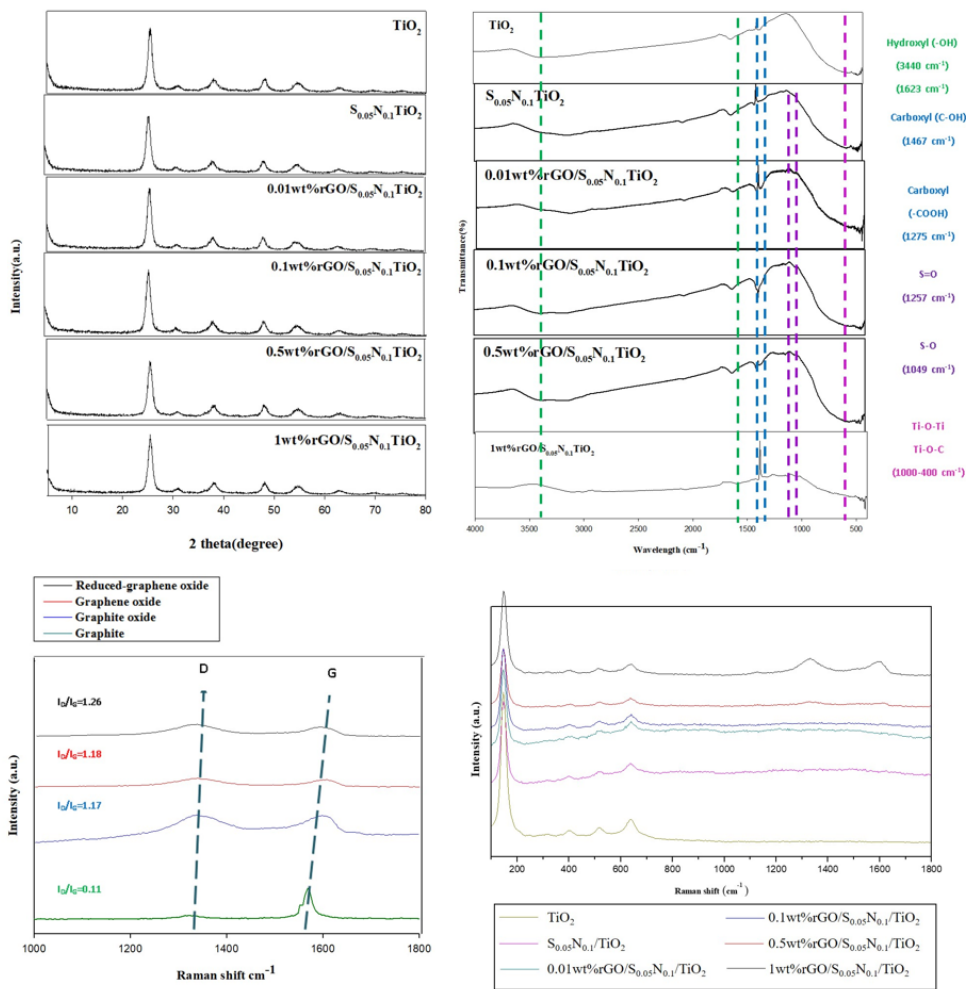


Figure 1

(a) XRD patterns, (b) FTIR spectra, and (c) raman spectra of various synthesized photocatalyst.

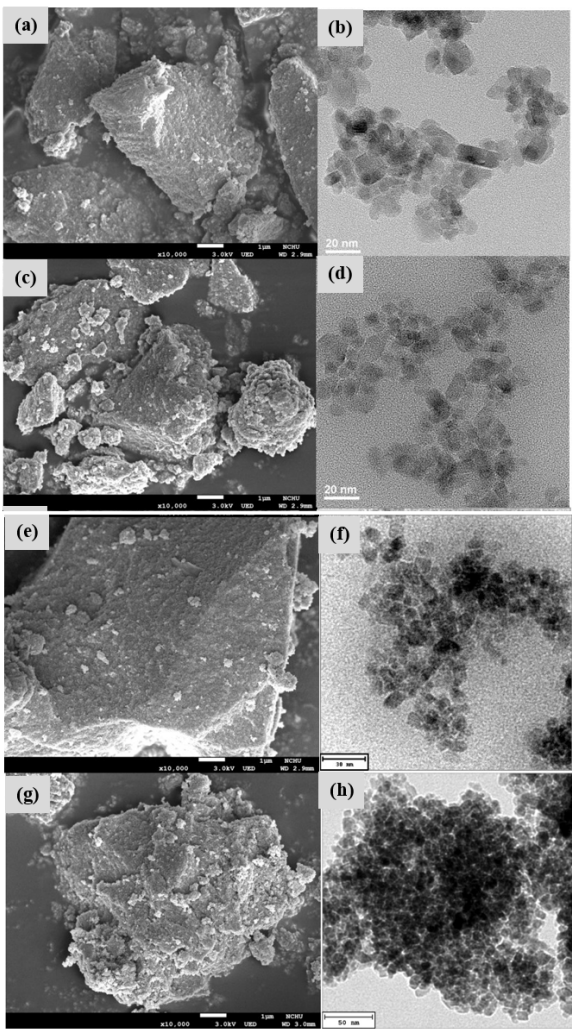


Figure 2

The SEM and TEM image of (a, b) TiO₂, (c, d) S0.05N0.1TiO₂, (e, f) 0.1wt%rGO/S0.05N0.1TiO₂, and (g, h) 1wt%rGO/S0.05N0.1TiO₂

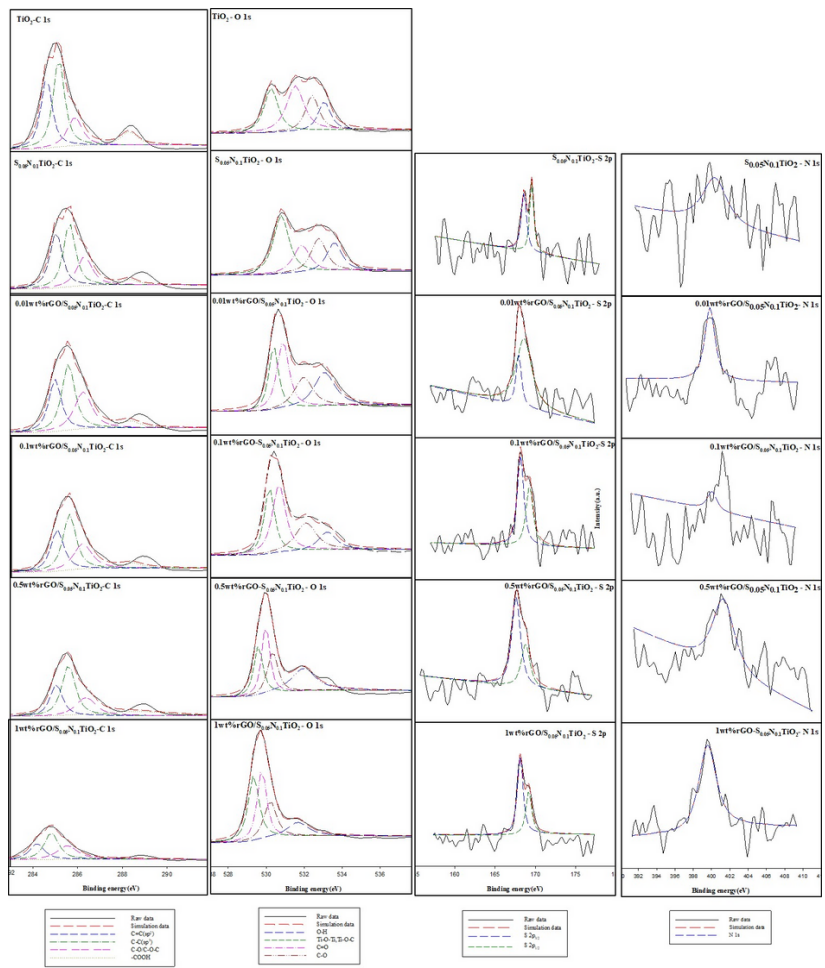


Figure 3

XPS spectra of various photocatalyst

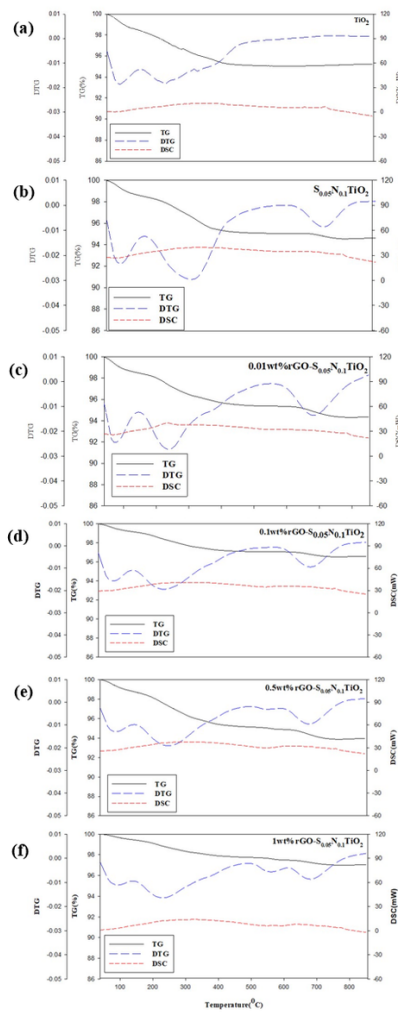


Figure 4

(a) TiO_2 , (b) $\text{S}0.05\text{N}0.1\text{TiO}_2$, (c) 0.01, (d) 0.1, (e) 0.5, (f) 1, (g) 5wt%rGO/ $\text{S}0.05\text{N}0.1\text{TiO}_2$ TG-DTA curves.

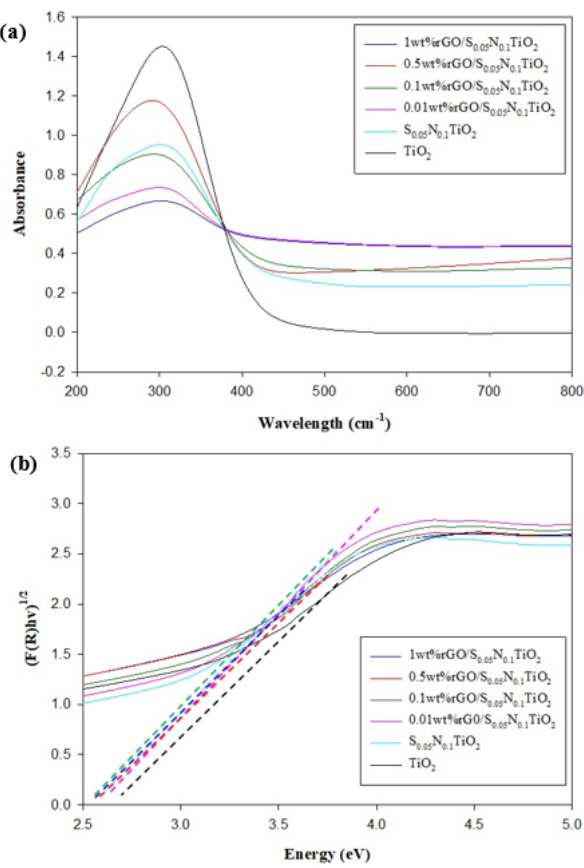


Figure 5

(a) absorbance spectra vs. wavelength and (b) diffuse reflectance spectra ($F(R)\cdot h\nu$)^{0.5} vs. energy for various photocatalysts.

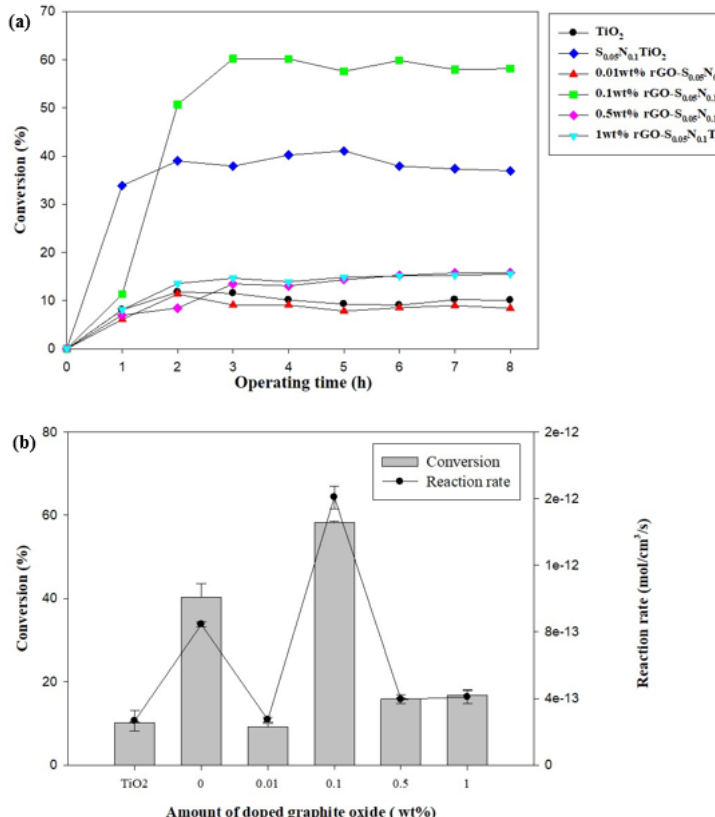


Figure 6

(a) conversion and (b) reaction rate value during the visible light-driven photocatalytic degradation process of toluene using synthesized photocatalyst.

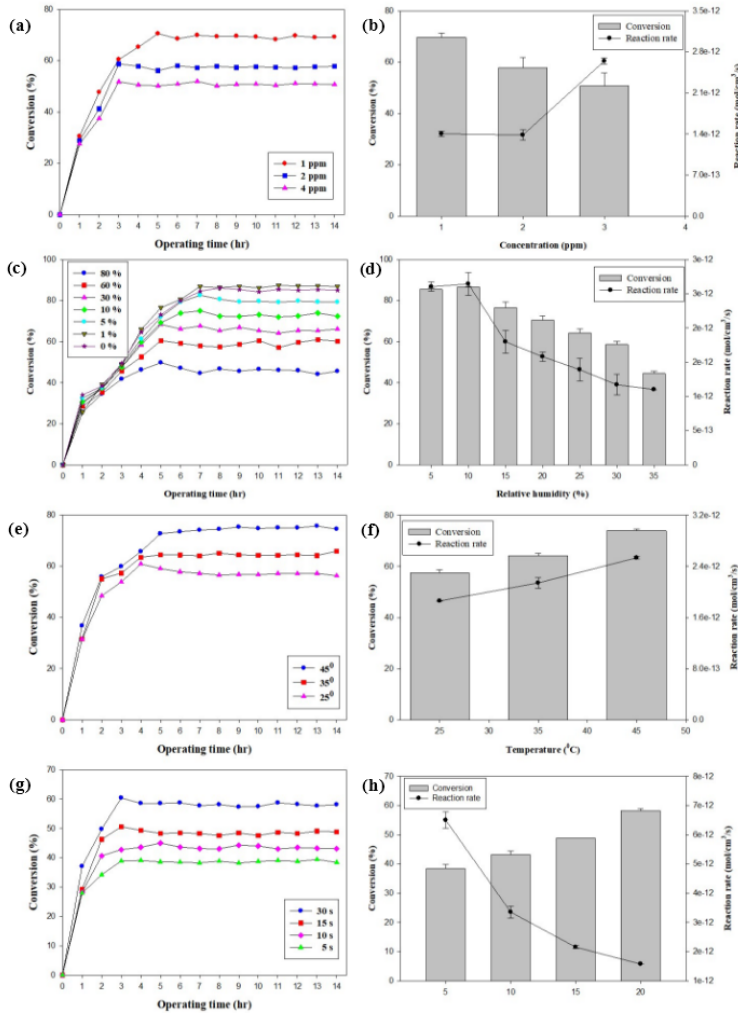


Figure 7

Photocatalytic degradation of toluene using 0.1wt%rGO/S0.05N0.1TiO₂ under various (a, b) initial concentration, (c, d) relative humidity (RH), (e, f) temperature, and (g, h) retention time.

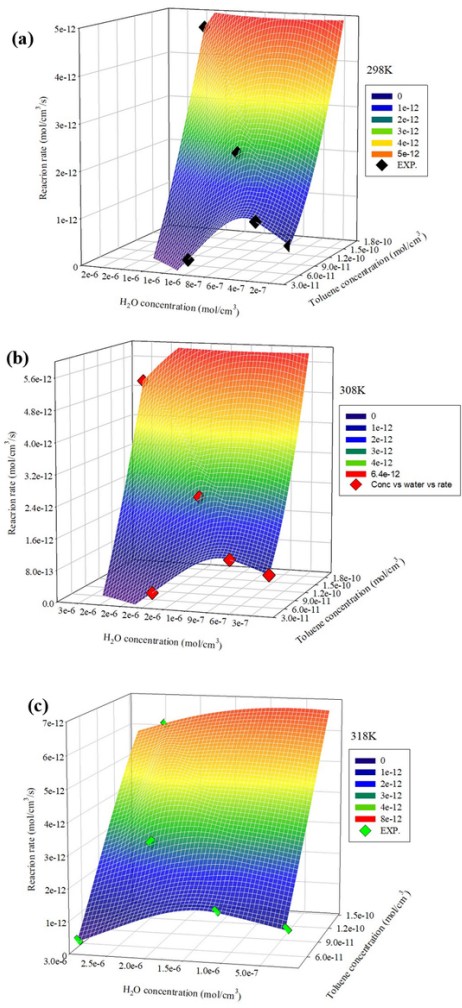


Figure 8

The predicted values and experimental values of reaction rate in 3D surface mesh using Langmuir-Hinshelwood models 4 at (a) 298, (b) 308 and (c) 318K.

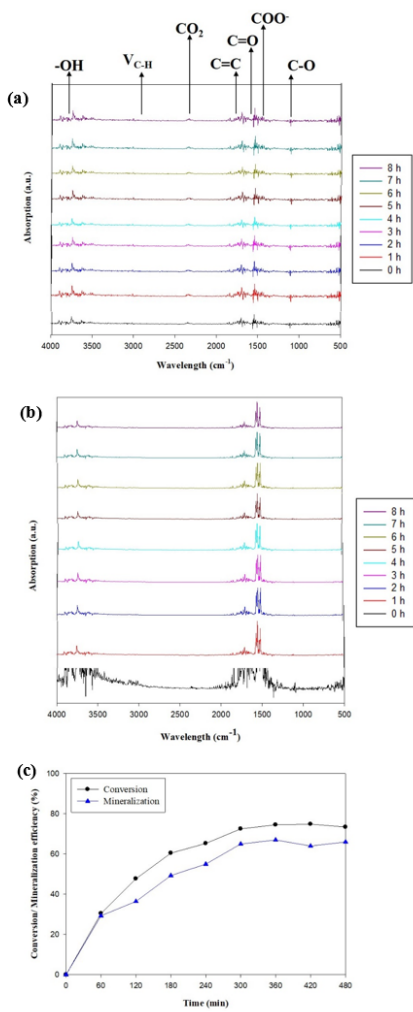


Figure 9

FTIR spectra of byproducts from toluene photocatalytic degradation under (a) 0% RH and (b) 60% RH by 0.1wt%rGO/S0.05N0.1TiO2 in the wavelength of 4,000-500 cm⁻¹ during 8 hours along with the (c) mineralization efficiency.

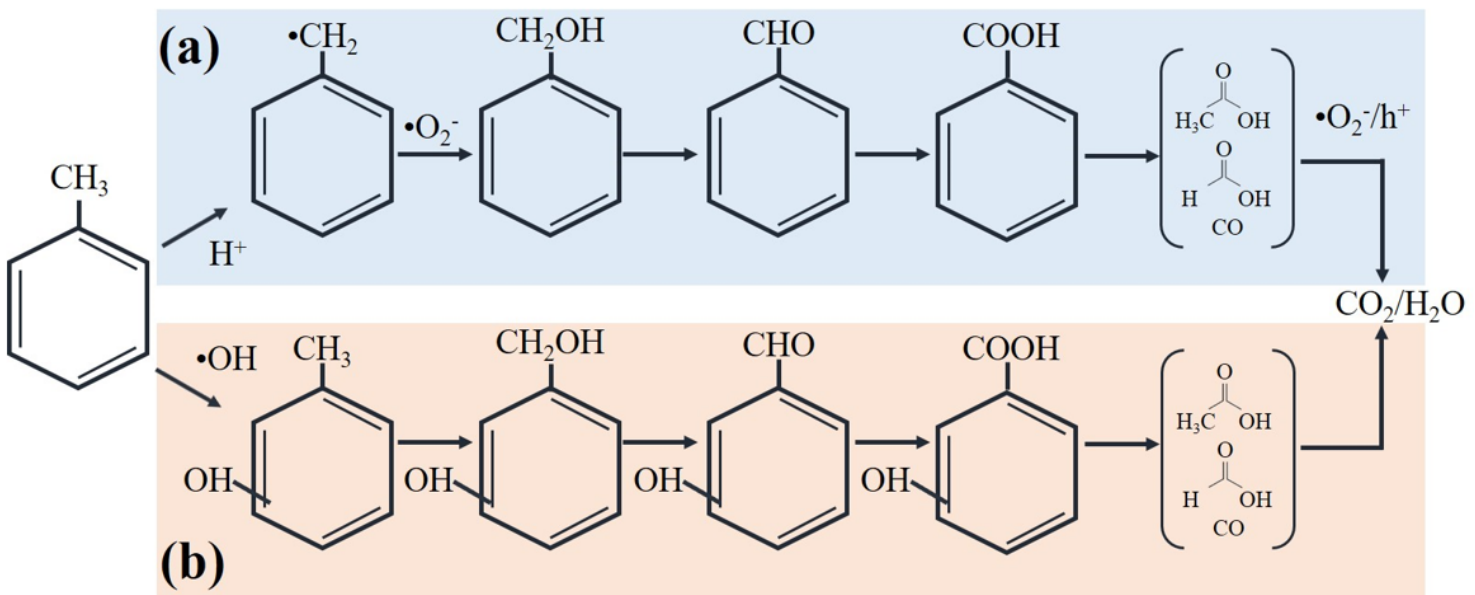


Figure 10

Predicted photocatalytic degradation of toluene under (a) 0%RH or (b) 60%RH.